

# Cenozoic India-Asia collision driven by mantle dragging the cratonic root

Received: 17 October 2023

Accepted: 29 July 2024

Published online: 06 August 2024

 Check for updates

Yanchong Li<sup>1</sup>, Lijun Liu<sup>2</sup>✉, Sanzhong Li<sup>3,4</sup>✉, Diandian Peng<sup>1,6</sup>,  
Zebin Cao<sup>1,7</sup> & Xinyu Li<sup>2,5</sup>

The driving force behind the Cenozoic India-Asia collision remains elusive. Using global-scale geodynamic modeling, we find that the continuous motion of the Indian plate is driven by a prominent upper-mantle flow pushing the thick Indian lithospheric root, originated from the northward rollover of the detached Neo-Tethyan slab and sinking slabs below East Asia. The maximum mantle drag occurs within the strong Indian lithosphere and is comparable in magnitude to that of slab pull ( $10^{13} \text{ N m}^{-1}$ ). The thick cratonic root enhances both lithosphere-asthenosphere coupling and upper-plate compressional stress, thereby sustaining the topography of Tibetan Plateau. We show that the calculated resistant force from the India-Asia plate boundary is also close to that due to the gravitational potential energy of Tibetan Plateau. Here, we demonstrate that this mantle flow is key for the formation of the Tibetan Plateau and represents part of a hemispheric convergent flow pattern centered on central Asia.

The continuous northward convergence of the Indian plate with Tibet after their Cenozoic (~50 Ma) collision<sup>1–3</sup> (Fig. 1, Supplementary Movie 1) represents a key linkage among the termination of the Neo-Tethyan ocean, the birth of the Indian Ocean, and the formation of Tibetan Plateau. In addition, geophysical analysis suggests that the late-Cenozoic resistance force due to the gravitational potential energy (GPE) of the Himalayas and Tibetan Plateau ranges from  $3 \times 10^{12} \text{ N m}^{-1}$  to  $8 \times 10^{12} \text{ N m}^{-1}$ <sup>4–7</sup>. Consequently, the force driving the northward convergence should be only higher than this value given the potential resistance from other boundaries of the Indian plate<sup>8</sup>. Yet, direct slab pull, the most commonly invoked plate driving force with a comparable amplitude ( $10^{13} \text{ N m}^{-1}$ )<sup>9</sup>, is largely negligible because of the absence of a continuous oceanic slab below the present collision zone<sup>10,11</sup>. Ridge push, on the other hand, is too small, given its typical amplitude of  $3 \times 10^{12} \text{ N m}^{-1}$ <sup>6,7,9</sup>. Thus, the post-collisional Indian motion cannot be adequately explained by the above mentioned plate driving

forces<sup>8</sup>, leading to the intriguing question of what the dominant driving mechanism and its associated origin are.

This problem has invoked multiple hypotheses. One of these refers to the continuous subduction of the continental lithosphere which is considered dense enough to provide an alternative slab pull force<sup>12,13</sup>. However, their predicted depth-continuous steep slab is at odds with the observed seismic structure where the Indian lithosphere is shallowly underplating Eurasia with no connection to prominent deeper slabs<sup>10,11,14,15</sup>, not to mention the likely early formation of eclogite densification<sup>16</sup> and the early slab breakoff<sup>17</sup>. Another proposal suggests that nearby subducting plates like the Capricorn and Australian plates transmit far-field slab pull from below Southeast Asia to the Indian plate interior<sup>7,18–21</sup>, but this mechanism is dynamically challenging for neighboring plates with near-parallel motion directions<sup>22</sup>, especially for a force large enough to overcome the substantial GPE-induced resistance from Tibet.

<sup>1</sup>Department of Earth Science and Environmental Change, University of Illinois at Urbana-Champaign, Urbana, IL, USA. <sup>2</sup>State Key Laboratory of Lithospheric Evolution, Institute of Geology and Geophysics, Chinese Academy of Science, Beijing, China. <sup>3</sup>Frontiers Science Center for Deep Ocean Multispheres and Earth System, Key Lab of Submarine Geosciences and Prospecting Techniques, MOE and College of Marine Geosciences, Ocean University of China, Qingdao, China. <sup>4</sup>Laboratory for Marine Mineral Resources, Qingdao Marine Science and Technology Center, Qingdao, China. <sup>5</sup>Laboratory of Seismology and Physics of Earth's Interior, School of Earth and Space Sciences, University of Science and Technology of China, Hefei, China. <sup>6</sup>Present address: Scripps Institution of Oceanography, UC San Diego, La Jolla, CA, USA. <sup>7</sup>Present address: State Key Laboratory of Lithospheric Evolution, Institute of Geology and Geophysics, Chinese Academy of Science, Beijing, China. ✉e-mail: [ljiu@mail.iggcas.ac.cn](mailto:ljiu@mail.iggcas.ac.cn); [sanzhong@ouc.edu.cn](mailto:sanzhong@ouc.edu.cn)

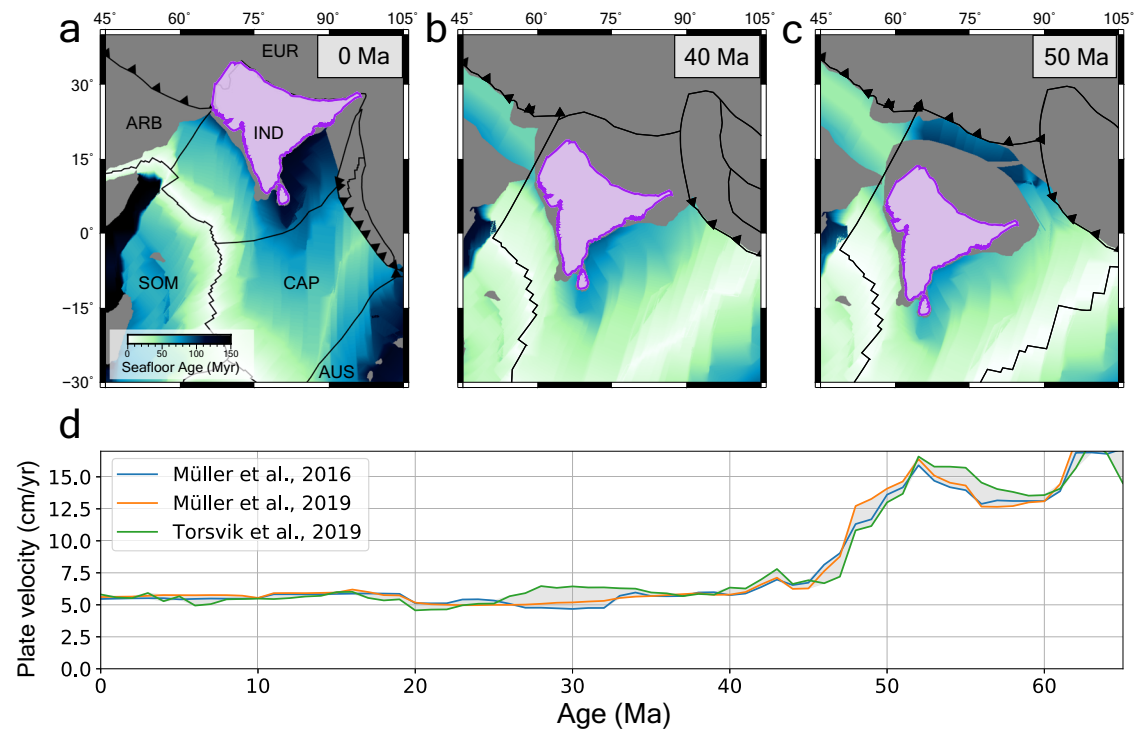


**Fig. 1 | Cenozoic Indian configuration and plate motion.** **a–c** Plate reconstruction at 0, 40, and 50 Ma, respectively<sup>3</sup> showing the history of continent-continent collision. Gray areas represent continental regions. Black lines delineate major tectonic boundaries. Among them, subduction zones are represented with triangular arrows showing subduction directions. ARB: Arabian plate, AUS: Australian plate,

CAP: Capricorn plate, EUR: Eurasian plate, IND: Indian plate, SOM: Somalian plate. **d** Cenozoic Indian plate speed in the no-net-rotation (NNR) reference frame from three different reconstructions<sup>3,68,69</sup>. Gray areas demonstrate the range of reconstructed Indian plate speed.

A conceptually more feasible driving force is the mantle drag from the faster-moving asthenosphere acting at the bottom of the lithosphere<sup>23–26</sup>, where the associated fast mantle flow was proposed to be induced either by a rising plume<sup>26</sup> and/or suction of foundered slabs<sup>25</sup>. However, many aspects of this driving force remain unclear, such as its amplitude and duration, how the asthenosphere interacts with the lithosphere, the physical origin of the fast mantle flow, and its capability to maintain both plate motion and the India–Asia collision.

In this work, we address these questions using a global, time-dependent geodynamic model that couples the lithosphere and the convective mantle. We further quantify both the driving and resisting forces within the model. Through a systematic and quantitative analysis of the entire dynamic system, we demonstrate that mantle drag is the dominant driving force behind the Cenozoic India–Asia collision and the motion of the Indian plate.

## Results

### Cenozoic slab evolution and mantle flow

We tackle these problems using a global, sequential-in-time data-assimilation model starting from 200 Ma (see Method for more details) based on a recent plate reconstruction<sup>3</sup>. This model generates evolving mantle structures (Supplementary Fig. 1) including slabs and large-low-shear-velocity provinces (LLSVPs) that match present-day tomographic structures both regionally (see below) and globally<sup>27–30</sup>. Its temporally evolving continental lithospheric thickness in response to mantle dynamics also allows quantifying the lithosphere–asthenosphere interaction due to the variable lithosphere–asthenosphere boundary (LAB) depth (Supplementary Fig. 1c, d), as recently done<sup>31–33</sup>. To reproduce observed plate motion at different times using a fully dynamic approach, we solve the flow using the corresponding mantle structures from the data-assimilation model while allowing the surface to deform freely in the horizontal directions.

During this calculation, we also vary the effective viscosity values of the plate boundaries and the oceanic asthenosphere, both of which are not well determined during the initial sequential simulation. After obtaining a satisfactory match between modeled and observed plate motion at the present, the same viscosity adjustment is applied to all other times (see Method). Finally, based on these results we analyze the properties and origin of the relevant forces.

Our model's reproduction of present-day global plate motion (Fig. 2a) is comparable to, or better than published results<sup>19,25,34</sup>. As a step further, our calculation also properly reproduces the past motions of the Indian plate (Figs. 2b, c, and 4c). A prominent dynamic feature is that the asthenospheric flow south of the Indian continent is consistently much faster than the surface plate motion. The good fit between modeled (see Method) and observed asthenospheric (200 km depth) seismic anisotropy (Fig. 2d) further supports the directionality of this fast mantle flow. These results indicate that the previously hard-to-quantify viscous mantle drag should act as an important driving force for the persistent Cenozoic Indian plate motion.

In our model, the faster-than-surface asthenospheric flow is a direct result of the lateral dynamic pressure gradient in the upper mantle, where the pressure is high beneath the southern Indian Ocean and low beneath the Indian continent (Fig. 3b). This pressure gradient exerts a net force pushing the mantle to go northward, generating a type of flow called the Poiseuille flow<sup>29</sup>. Consequently, the overriding Indian lithosphere, which moves more slowly due to resistance from its boundaries, especially on the northern side, experiences a mantle drag from the fast-moving asthenosphere below it.

The low-pressure upper mantle beneath the Indian continent is a combined result of (1) the sinking and southward rollover of the Neo-Tethyan slab in the mid-lower mantle, and (2) the voluminous slab pile beneath Eurasia at lowermost mantle depths comprising both the Neo-

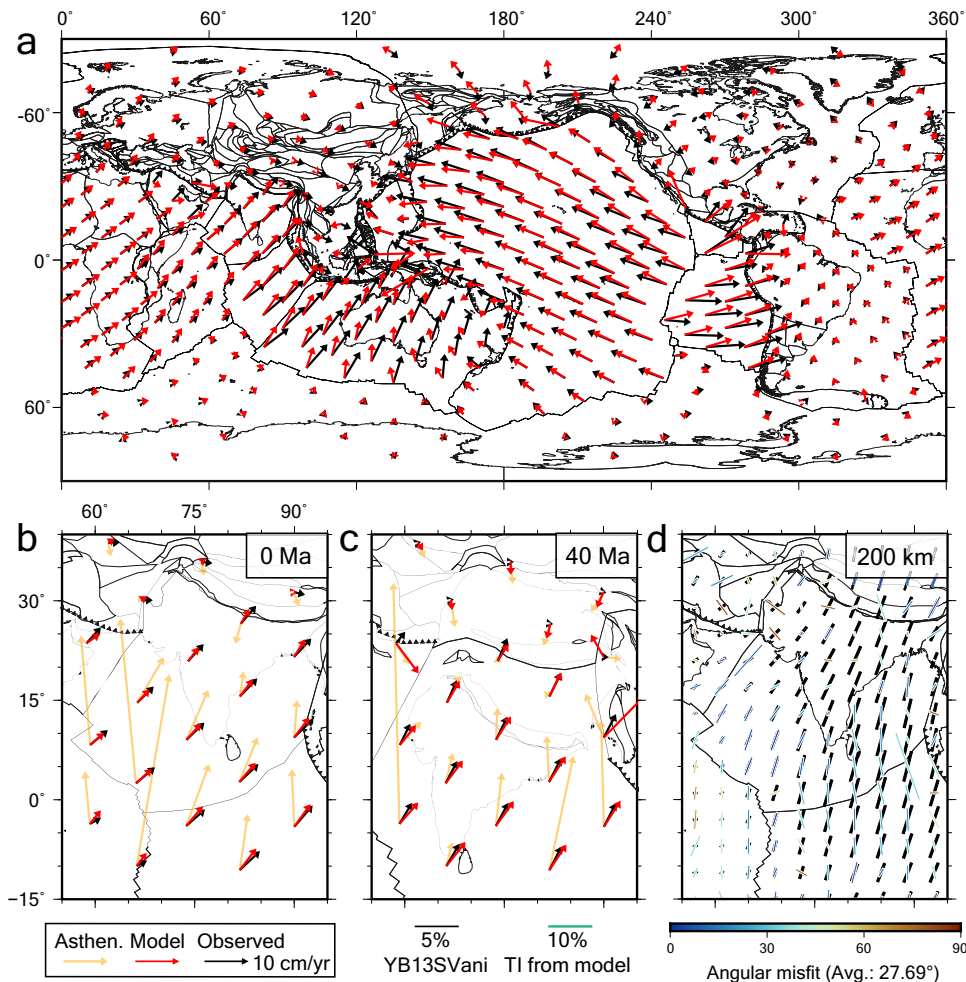


**Fig. 2 | Plate motion, asthenospheric flow, and anisotropy comparison.**

**a–c** Comparison between modeled plate motion and that from the reconstruction<sup>3</sup>, as well as asthenospheric flow in **b** and **c**. The shown asthenospheric flow is the maximum upper-mantle velocity below the lithosphere. All velocity here is based

on the NNR reference frame. Black and gray lines delineate major tectonic boundary and coastline. **d** Comparison between modeled (lines color-coded by angular misfit) and observed anisotropy (black lines), based on the model YB13SVani<sup>70</sup>. TI represents the symmetry axis of the transverse isotropy.

Tethyan and Izanagi slabs<sup>27</sup>. The southward rollover of the sinking Neo-Tethyan slab at lower-mantle depth, caused by continuous trench advance, reduces the pressure beneath the subducting plate instead of the overriding plate, with the latter being more commonly observed with retreating slabs. The relatively high pressure in the upper mantle south of the continent is partly due to the upwelling plume from the underlying African LLSVP. Both the subducted slabs and upwelling plumes are consistent with seismic tomography (Fig. 3a).

The amplitude of dynamic pressure and its lateral gradient scale linearly with the density anomalies and only weakly depend on mantle viscosity, for a given spatial pattern of mass distribution<sup>35</sup>. This property allows us to estimate the relative contributions of various density anomalies to the observed present-day plate motion and associated mantle drag, without worrying about the effect of mantle viscosity. Compared to the Eurasian slab pile, the Neo-Tethyan slab is less voluminous, thus its removal only slows the Indian plate by ~20% (Supplementary Figs. 2c, 3b). However, in this case, the Eurasian plate moves northward much faster at a similar rate to India, implying little convergence between the two plates. Removing lower mantle slabs globally will stop the mantle flow and its driving of the Indian plate (Supplementary Figs. 2f, 3c), consistent with the scenario where both slab pull and slab suction are absent<sup>25</sup>. Thus, both slab piles are essential in driving Indian convergence: while the voluminous Eurasian slab pile generates regional-scale low pressure below central-eastern

Asia, the Neo-Tethyan slab interjects to expand the low-pressure center to below north India and generate the proper asthenosphere flow pattern associated with the observed India–Tibet convergence (Fig. 3b). The dense continental eclogite (see below) existing in all three cases have only minor impact on the large-scale mantle flow. This highlights a complex multiscale interaction among the sinking mantle slabs that is hard to illustrate in simpler models used previously.

As a further step from earlier studies, the time-dependent nature of our model allows us to examine the evolution of the slab and its control on the mantle flow during the geological past. The detachment of the Neo-Tethyan slab happened between 50 Ma and 40 Ma after the closure of the Neo-Tethyan ocean (Fig. 3d, e). In contrast to the traditional slab suction hypothesis<sup>25,36</sup>, the faster-than-surface upper-mantle flow appeared even before the slab detachment (Fig. 3d). This flow was likely attracted by the Izanagi subduction in the north, which also induced the Neo-Tethyan trench advance and slab rollover. This fast asthenospheric flow persists from >50 Ma to the present day, suggesting a consistent driving force for the Indian plate throughout the post-collision Cenozoic era. In the following section, we quantify this driving force and demonstrate its dominant contribution to the India–Asia collision.

### Mantle drag due to lithosphere–asthenosphere interaction

While some previous research suggested mantle flow as a potential driving mechanism for the post-collisional Indian motion<sup>23,26,37</sup>, the

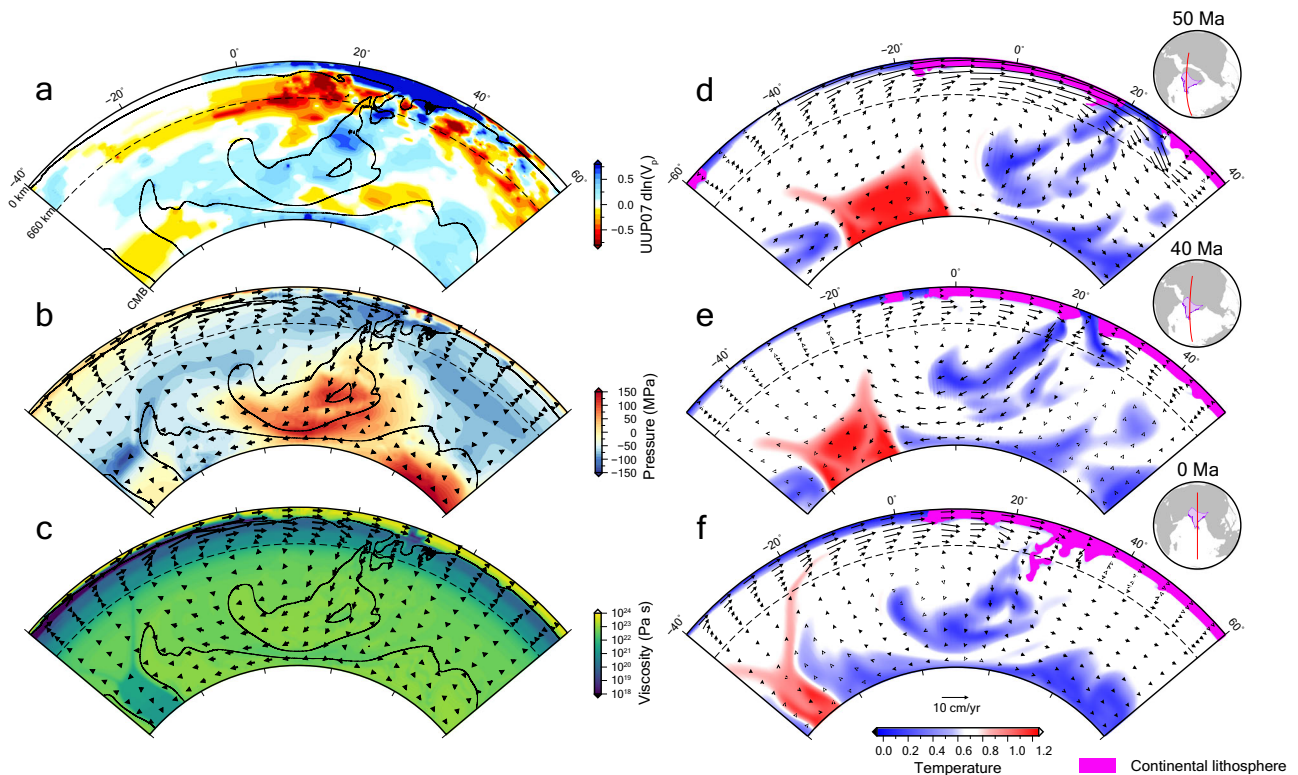


**Fig. 3 | Neo-Tethyan slab evolution and viscosity, dynamic pressure in model and tomography.** **a** Comparison between the tomography UUP07<sup>11</sup> and modeled slab structure (dark contour denotes the 0.6 non-dimensional temperature volume). **b** Modeled dynamic pressure at 0 Ma. **c** Modeled viscosity structure at 0 Ma. Note that the collisional plate boundary between India and Eurasia at  $\sim 30^\circ$  N is fully weakened in the entire lithospheric depth. The velocities in **b** and **c** are from

free-slip models and follows a no-rigid-rotation reference frame. This reference frame set global three-dimensional mantle rotation to 0. **d–f** Modeled mantle evolution tracking the Indian collision process with mantle velocity. The velocities here are from the impose plate motion model and follows the reference frame used in the plate reconstruction<sup>3</sup>.

existence, magnitude, distribution, and evolution of this force all remain unclear. For example, the much lower (by many orders of magnitude) asthenospheric viscosity than that of the overlying lithosphere seems to dismiss mantle drag as a major driving force<sup>38,39</sup>. Thicker lithospheric keels could affect the coupling between the lithosphere and the underlying mantle<sup>23</sup>, but this effect on continental motion is uncertain<sup>8,39,40</sup>, due to its strong dependence on the poorly constrained mantle flow pattern. Therefore, it is necessary to further quantify the flow-induced mantle drag and how the asthenosphere interacts with the lithosphere with the presence of a weak asthenosphere and variable LAB depth in an evolutionary model.

Mantle drag consists of two types (Fig. 4a, b): (1) Friction drag due to shear stress along the lithosphere boundary, and (2) pressure drag due to force normal to the contact surface through pressure gradients. Inside the convecting Earth, friction drag originates from the vertical gradient of horizontal flow around the base of the lithosphere, while pressure drag mostly occurs along lithospheric steps where the LAB depth varies laterally. Our analysis (Method) shows that the magnitude of total mantle drag along the plate motion direction is  $1.1 \times 10^{13} \text{ N m}^{-1}$  at present, exceeding the highest estimation ( $8 \times 10^{12} \text{ N m}^{-1}$ ) of Tibetan resistance from the northern plate boundary. Among these forces, friction drag has a dominant magnitude of  $8.8 \times 10^{12} \text{ N m}^{-1}$  while pressure drag is  $2.2 \times 10^{12} \text{ N m}^{-1}$  (Fig. 4a, b).

Interestingly, both friction drag and pressure drag show a prominent concentration around the southwestern edge of the Indian continent, where a large lithospheric step exists. This concentration accounts for  $\sim 50\%$  of the total friction drag and nearly 100% of the pressure drag. Spatially, this lithospheric step corresponds to a sharp slowdown of the asthenospheric flow that is blocked by the thicker continental keel to the northeast (Fig. 2b). This observation confirms

the important role of a thicker lithospheric root for increasing coupling between the plate and the asthenosphere<sup>23,32,39</sup>.

The resistant force acting on the northern plate boundary is  $9.7 \times 10^{12} \text{ N m}^{-1}$  at present-day (Fig. 4b), comparable to the total mantle drag as well as the GPE estimation ( $3 \times 10^{12} \text{ N m}^{-1}$  to  $8 \times 10^{12} \text{ N m}^{-1}$ )<sup>4–7</sup>. This means that most of the driving force is balanced by the collisional resistance from the India–Asia collision. The largest resistant force is located in the mid-western part of the collision zone, likely as a direct reaction along the plate motion direction to the large driving force from the southwestern edge of the Indian continent. This shows that our model, although not explicitly including a free surface to mimic the high plateau topography, captures the correct sub-surface vertical stress along the plate boundary that represents the correct GPE as occurred in reality.

In contrast to the traditional view that a weak asthenosphere diminishes the mantle drag<sup>38,39</sup>, our results demonstrate that the maximum shear stress occurs within the relatively strong lithospheric root (Supplementary Fig. 4a). Inside the weak asthenosphere, the maximum friction drag is about half of that within the lithosphere above (Supplementary Fig. 4b, c), much greater than that implied from a linear proportion scaled with viscosity, as previously found<sup>39</sup>. In general, the effective mantle drag gradually increases from the weak asthenosphere to the strong lithospheric interior, irrespective of their viscosity contrast.

However, reducing the asthenospheric viscosity does help decouple the plate from the underlying mantle. A set of models with uniform lithospheric thickness but varying asthenospheric viscosity confirm this effect (Supplementary Fig. 5), where the mantle drag decreases by a factor of 2.5 (from  $5 \times 10^{12} \text{ N m}^{-1}$  to  $2 \times 10^{12} \text{ N m}^{-1}$ ) as asthenospheric viscosity drops by a factor of 20 (from  $1 \times 10^{20} \text{ Pa s}$  to

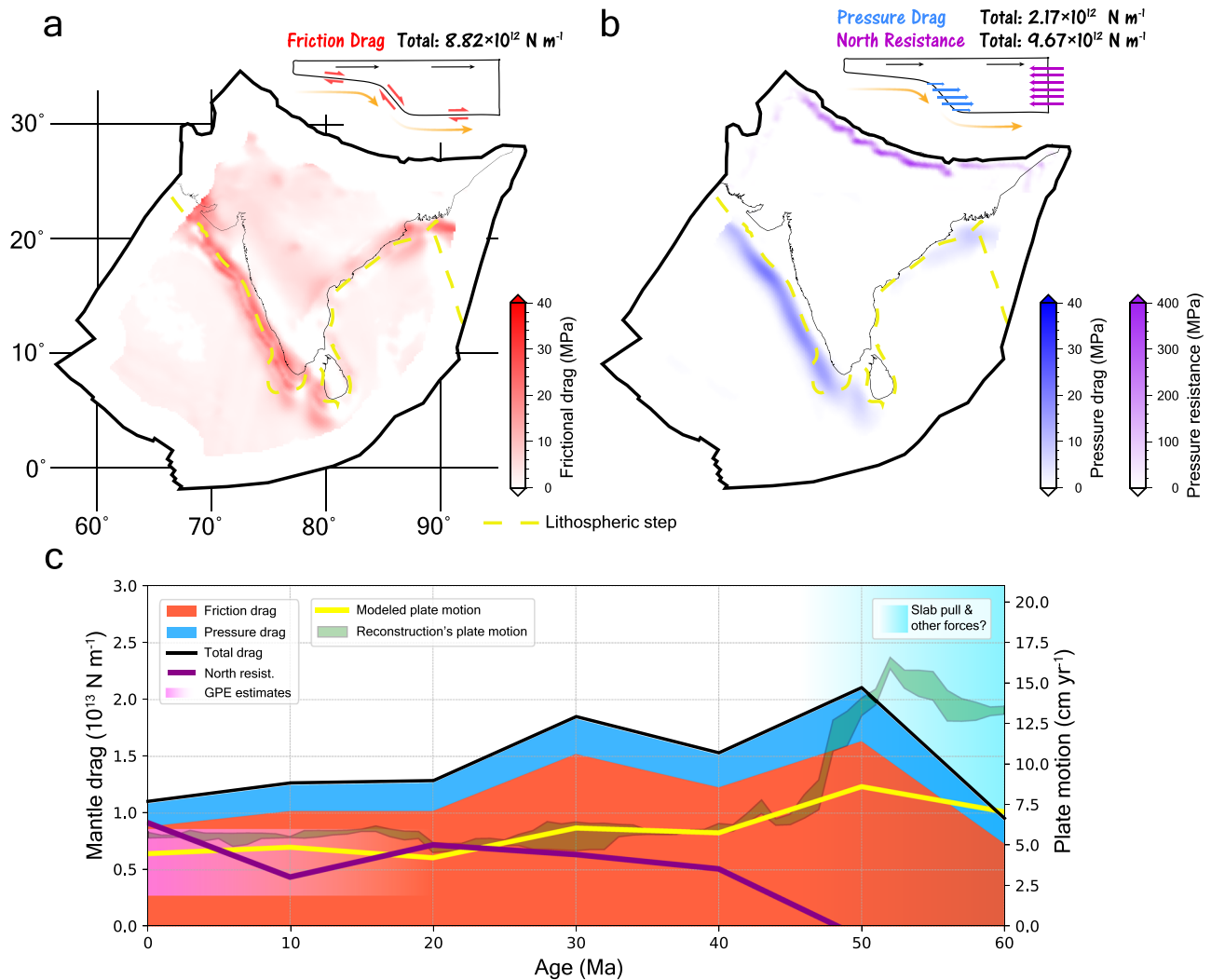


**Fig. 4 | Quantification of two types of mantle drag and their evolution.** **a** Friction drag schematic and its modeled distribution within the Indian plate. **b** Pressure drag and northern boundary resistance schematics and their modeled distributions within the Indian plate. A unit of force per area is chosen for better comparison to friction drag. Note the scale difference between drag and resistant force. Both friction drag and pressure drag are projected to the plate motion direction. **c** Evolution of modeled mantle drag (colored areas), northern Indian boundary

resistance, observed (from Fig. 1d) vs predicted plate motion history during the Cenozoic (line features) in the NNR reference frame. The purple curve shows the resistant force from continental collision in the north of the Indian plate. Note that it may not reflect full northern resistance before 40 Ma given the slab is still attached to the lithosphere acting as a stress guide. The gradational cyan region prior to 45 Ma represents other potential driving forces not considered in our model.

$5 \times 10^{18} \text{ Pa s}$ ), consistently below the level of resistance force due to Tibetan GPE. On the other hand, further increasing the asthenospheric viscosity will lead to a saturation in the magnitude of mantle drag (see the relative change in asthenospheric viscosity and mantle drag in Supplementary Fig. 5). This result further confirms the previous finding that, for a given density distribution, buoyancy has a much stronger control on sub-lithospheric stress than mantle viscosity<sup>35</sup>. Consequently, lithospheric thickness variation must contribute additionally to balance the resistance from the Tibetan Plateau.

Previous studies adopting a uniform lithospheric thickness were able to reproduce the present Indian motion<sup>26</sup>, thus raising a question on the respective roles of friction drag, pressure drag, and Tibetan resistance. To explore these forces and the resulting plate motion predictions, we successively reduce the thickness of the continental root. This reduction leads to progressively smaller mantle drags (Supplementary Fig. 6a–c) that eventually fall below the threshold of Tibetan resistance ( $3 \times 10^{12} \text{ N m}^{-1}$ )<sup>6</sup>. With the maximum root depth being 200 km (250 km in the reference case), the Indian plate motion decreases slightly due to a smaller drag of  $8.4 \times 10^{12} \text{ N m}^{-1}$

(Supplementary Fig. 6a). However, truncating the root below 175 km leads to an increase in plate velocity although the drag is even smaller ( $6.8 \times 10^{12} \text{ N m}^{-1}$ ; Supplementary Fig. 6b). This increase of velocity may be attributed to the greater reduction in plate boundary resistance than in mantle drag. If the Indian plate is of a uniform thickness of 100 km (as in a previous study<sup>26</sup>), while the predicted plate motion remains acceptable, the mantle drag falls below the lowest estimate of Tibetan resistance ( $2.1 \times 10^{12} \text{ N m}^{-1}$  compared to  $3 \times 10^{12} \text{ N m}^{-1}$ ; Supplementary Fig. 6c). These results further suggest that the continental root affects the transmission of mantle drag into the overlying lithospheres in two ways: (1) to couple the Indian plate with the underlying asthenosphere, and (2) to maintain a large contact area between Indian and Eurasian plates. Thus, the continental root strongly modulates the balance among the mantle drag, the Indian plate motion, and the northern boundary resistance from the Tibetan Plateau. A recent study shows that the craton is compressed by mantle convection<sup>41</sup>, which is similar to our study except that one side of the cratonic India is sustained by continental collision. Since the mantle drags concentrate on the root edge that faces the fast mantle flow, the exact geometry of the

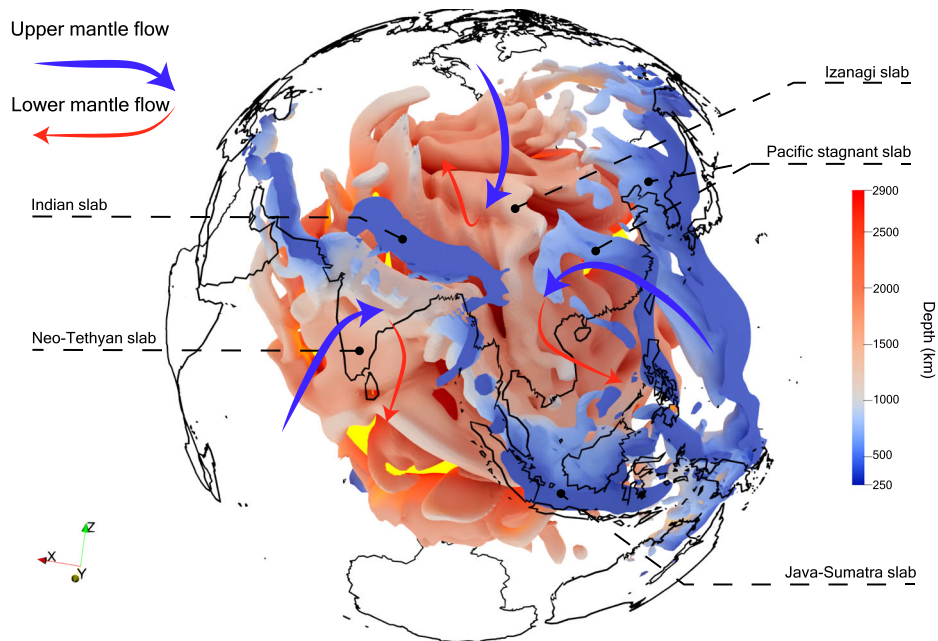


**Fig. 5 | Modeled East Asian slabs and hemispheric converging flow.** The blue-to-red volumes are present-day slabs with a temperature  $150\text{ }^{\circ}\text{C}$  lower than the ambient mantle at  $>250\text{ km}$  depth. Arrowed curves indicate the pattern of depth-dependent mantle flow from three different directions corresponding to three

subduction zones. The glowing yellow layer is the core-mantle boundary. Black lines represent coastlines. All major slabs are annotated. See Supplementary Movie 2 for 3D streamlines and the velocity field.

root will unlikely affect the overall coupling as long as the flow-normal area of the edge remains similar.

While some researchers suggest that the upwelling plume has a strong impact on mantle drag in this region<sup>26</sup>, our model reveals that the plume arising from the edge of the African LLSVP (Fig. 3f) does not significantly affect dynamic pressure beneath the Indian plate (Fig. 3b). To further examine the effect of mantle upwelling, we perform a test by removing all hot mantle anomalies in the model. Surprisingly, the reproduced Indian plate motion remains similar, and so does the amount of mantle drag (Supplementary Fig. 7). In addition, a recent seismic tomography study shows that the plume is mainly located beneath the Somalian plate, supporting its limited contribution to driving the Indian plate<sup>42</sup>. Therefore, we suggest that sinking slabs play a more crucial role than rising plumes in driving the Indian plate motion.

Following the same model setup that generates the preferred present-day forces (Fig. 4a, b) and kinematics (Fig. 2), we extend the analysis to the geologic past. The calculated mantle drag is consistently larger than the present-day value ( $-10^{13}\text{ N m}^{-1}$ ), with that at 50 Ma being twice as large (Fig. 4c). The calculated drag history closely follows the temporal trends of both predicted and observed plate motions since  $-45\text{ Ma}$  (Fig. 4c) when India-Asia collision started in the model (Fig. 1), further confirming mantle drag as the dominant driving force.

The modeled collisional resistance ranges from  $4.6 \times 10^{12}$  to  $9.7 \times 10^{12}\text{ N m}^{-1}$ , consistent with both present-day GPE estimates ( $3 \times 10^{12}$  to  $8 \times 10^{12}\text{ N m}^{-1}$ ) and the magnitude of mantle drag forces. The key finding is the overall consistency of the resistance force magnitude throughout the post-collisional period despite the fluctuation of resistance force at 10 Ma, which is induced by an active boundary-wise lithospheric delamination (Supplementary Fig. 8) temporarily guiding the collisional force downward. This consistency validates our results and agrees with geological evidence for the early Cenozoic uplift of the Tibetan Plateau<sup>43</sup>. The long-term compatibility between modeled forces and independent GPE estimates reinforces the robustness of our findings in capturing the first-order dynamics of the India-Asia collision.

Our estimated plate motion cannot reproduce the much faster Indian motion from 60 to 50 Ma. Both the small magnitude of mantle drag and the assumed single subducting slab (Fig. 3d) during this period implies the operation of other potential driving forces such as those discussed in the following section. The resistance force drops below zero in the pre-collisional snapshots. Because our quantification method does not fully account for the force transmitted through the strong, coherent slab attached to the subducting plate, the negative resistance probably represents a net force contributing to trench advance prior to the continental collision.

### Implications on forces driving plate motion and continental collision

The quantification of the Cenozoic mantle drag permits a reevaluation of other potential plate driving forces. Although our model assimilates lateral density variations of oceanic lithosphere following seafloor age, it likely does not fully capture the effect of ridge push due to the flat model surface across the spreading center. However, given its small magnitude of  $-3 \times 10^{12}\text{ N m}^{-1}$ <sup>9</sup> that cannot even overcome the minimum estimate in Tibetan GPE force<sup>6</sup>, ridge push is unlikely to be a major driving force for the Cenozoic Indian motion. We suggest this should be a secondary force that might contribute to explaining the slightly slower predicted plate motion compared to observation (Fig. 4c).

Additional results reveal that slab pull from nearby subduction<sup>7,18</sup>, specifically the Sumatra-Java slab pull (Supplementary Fig. 9) acting through the Indian-Capricorn plate (IND-CAP) boundary (Fig. 1a), should also be minor compared to mantle drag. In practice, the Indian mantle drag and the IND-CAP boundary drag are complementary forces in driving Indian plate motion. With weakened Indian plate boundaries (to minimize surrounding forces), a uniformly thick Indian lithosphere, and a weak asthenosphere (to minimize mantle drag), the Indian plate experiences nearly no motion (Supplementary Fig. 6d). Strengthening the IND-CAP boundary based on this model (Supplementary Fig. 6f) to allow the transmission of the Sumatra slab pull to India only produces a small fraction of the observed plate motion, similar to the scenario where the Indian continental root is thickened

by 50 km to increase the lithosphere-asthenosphere coupling (Supplementary Fig. 6e). Since these two models predict similar plate motions, the extra  $1 \times 10^{12} \text{ N m}^{-1}$  mantle drag in the latter model could approximate the amount of IND-CAP boundary drag in the former model, thus confirming its minor role in sustaining the Cenozoic Indian-Tibetan collision.

Our model does not reproduce the faster plate motion ( $> 10 \text{ cm yr}^{-1}$ ) observed before -50 Ma. This may imply the existence of other driving forces besides mantle drag. Relevant hypotheses include a rising plume head<sup>44,45</sup>, additional slab pull due to double subduction<sup>46</sup> and thinning of Indian lithosphere<sup>47</sup>. Our model does not produce a major plume around this time (Fig. 3d–f), thus not capturing this additional force. The plate reconstruction we adopted does not consider a double subduction scenario either – it instead incorporates a back-arc setting with a southward trench jump<sup>3</sup>. Model tests also show the reduction of lithospheric thickness can increase plate speed with small driving force (Supplementary Fig. 6b). Therefore, we propose that these alternative hypotheses were likely at play during the earliest Cenozoic.

The history of the India–Asia collision provides additional support for the underlying mantle drag as the dominant driving force. The estimated present-day southward resisting force from the Tibetan Plateau ( $3 \times 10^{12} \text{ N m}^{-1}$  to  $8 \times 10^{12} \text{ N m}^{-1}$ )<sup>4–7</sup> matches our estimated resistant force from the northern boundary since 40 Ma (Fig. 4c). It also provides a minimum estimate of the required amount of northward Indian plate driving force, substantiating the necessity of mantle drag acted on a thick continental root, since the amplitude of the mantle drag is notably larger than that of other relevant forces as discussed above. The India–Asia collision history was characterized by persistent northward advancement of the Neo-Tethyan subduction zone, which likely started in the Cretaceous when India was initially rifted off from Gondwana<sup>48</sup>. This phenomenon is unique among global plate tectonics where most oceanic trenches tend to roll back. Our results show that a strong northward mantle drag existed even before the onset of collision (e.g., 50 Ma, Fig. 1c). This drag not only maintains the Indian motion but also carries the trench northward, which is a dynamic feature that has not been addressed in most previous studies.

## Discussion

What sets our findings apart from previous studies is the identification of a plate-scale convection cell spanning the entire mantle depth below India. This convection cell is part of a broader hemispheric convergent flow pattern at the upper-middle mantle depth centered primarily below Tibet (Fig. 5, Supplementary Movie 2). The trajectory of the subducting Neo-Tethyan slab outlines the larger-scale flow structure at its southern edge, with upper-mantle northward and lower-mantle southward motions. This unique flow pattern is mostly independent of the detailed tectonic setting between the Indian Plate and the Tibetan Plateau during their collision, but instead controlled by the long-term (since the early Mesozoic) subduction history within the eastern hemisphere, where the Tethyan, Paleo-Pacific, and Paleo-Mongolian plates have subducted beneath Eurasia from the south, east, and north, respectively<sup>3</sup>.

Recently, we showed that this multi-slab dynamic system progressively decreased the dynamic pressure below East Asia during the late Mesozoic, firstly leading to the formation of a Late-Cretaceous continental-scale flat Izanagi slab<sup>28</sup>, and subsequently forming the stagnant slabs below East Asia<sup>29</sup>. Further south and east around the East Asian margins, the same flow regime may also explain the rapid northward motion of the Australian plate<sup>3</sup>, as well as the formation of back-arc basins along the entire west Pacific margin<sup>31</sup>, all occurring in the Cenozoic. This dynamic effect is also similar to that driving the westward motion of North America<sup>49</sup>.

Therefore, the Cenozoic India–Asia collision is just one of the multiple tectonic expressions of this hemispheric convergence flow pattern. Unlike other circum-Asia regions where the abutting tectonic plates are wide, the Neo-Tethyan-Indian plate is narrow in the

east-west direction bounded by transform faults and mid-ocean ridges (Supplementary Movie 1). Its unique geometry and location above the conjunction of the Tethyan-Pacific subduction zones allow it to respond more readily to the underlying mantle drag. This property shapes the unique northward Indian kinematic history, the special rollover geometry of the Neo-Tethyan slab, and the resulting persistent continent-continent collision forming the Tibet Plateau. We propose that this long-lasting hemispheric convergence should represent an important driving force for the one-way tectonic train closing the Tethyan belt<sup>50</sup>, and may also eventually lead to the formation of the next supercontinent around Eurasia<sup>51</sup> by transforming the current degree-2 global mantle flow pattern to a degree-1 configuration<sup>52</sup>.

Previous research suggests that mantle models based on a free-slip surface boundary condition generate less realistic topography compared to free-surface models<sup>53</sup>. To investigate the impact of these boundary conditions on the force balance, we performed additional idealized tests using a free-slip model and a free-surface model (see Methods) and quantified the first-order stress distribution (Supplementary Fig. 10). We observed remarkably similar force profiles between the two models (Supplementary Fig. 10a), indicating that the underlying driving force remains comparable despite some local difference in the topography profile along the continental collision zone (Supplementary Fig. 10b). This similarity is further supported by the nearly identical mantle flow and plate motion distribution between the two models (Supplementary Fig. 10c, d), suggesting a similar stress distribution and consistency with previous reports<sup>54</sup>.

The stronger fluctuations generated in the free-slip model can be considered an unsmoothed version of the topography from the free-surface model, where small-wavelength fluctuations do not dictate the major force distribution. The overall similarities between topography and forces are of a wavelength much larger than the resolution of the global model (25 km). From a mechanical perspective, a free-slip boundary, despite having a flat surface, stores a finite vertical stress component that is equivalent to the stress at the same depth in a free-surface model. This equivalence implies that their respective GPE distributions are also similar. Based on these findings, we conclude that our global free-slip model is sufficient for determining the overall force balance within the lithosphere, as it captures the essential features of the stress distribution.

Our study employs an advanced data-assimilation approach to modeling mantle evolution by utilizing plate reconstructions rather than by directly defining the present-day mantle structures, i.e., converted from seismic tomography. This approach reproduces not only the temporal evolution of mantle dynamics but also the present mantle structures, thus matching more data constraints compared to those based on instantaneous calculations<sup>26</sup>. Additionally, our model incorporates lateral variations in lithospheric thickness, particularly the distinction between oceanic and continental lithosphere, instead of assuming a uniform thickness. This allows for a more accurate representation of the dynamics and stress distribution within the lithosphere, as shown in the effect of the lithospheric step in enhancing the driving force.

However, it is also important to acknowledge the limitations of our study. Our conclusions are constrained by the available observations, which may not capture all relevant processes at various spatial and temporal scales. While our global numerical model has a relatively high resolution, there is still room for improvement in resolving finer-scale processes, including realistic deformation within the continents and more complex interactions at plate boundaries. Despite these limitations, the consistency between our modeled force balance and observations supports our conclusions. Future work with higher numerical resolution and more realistic physical parameterizations will help to refine our understanding of the complex lithosphere-mantle coupling through deeper time.

## Methods

### Governing equations and data-assimilation

The global spherical geodynamic model is based on the code CitcomS<sup>55</sup>. The mantle is divided into 12 caps, each with a high-resolution mesh consisting of  $257 \times 257 \times 113$  nodes, equivalent to a horizontal (vertical) resolution of 25 km (12 km) near the surface. This resolution allows a proper capture of the lithospheric structure, especially its interaction with the convective mantle. We assume the mantle is incompressible and satisfies the Boussinesq approximation. The model simulates subduction history and mantle evolution through the last 200 Myr. The conservation equations for mass, momentum, energy, and chemical particles are:

$$\nabla \cdot \mathbf{u} = 0 \quad (1)$$

$$-\nabla P + \nabla \cdot \left[ \eta (\nabla \mathbf{u} + \nabla^T \mathbf{u}) \right] + (\rho_m \alpha \Delta T + \Delta \rho_c) \mathbf{g} = 0 \quad (2)$$

$$\frac{\partial T}{\partial t} + \mathbf{u} \cdot \nabla T = \kappa \Delta T \quad (3)$$

$$\frac{\partial C}{\partial t} + \mathbf{u} \cdot \nabla C = 0 \quad (4)$$

where  $\mathbf{u}$  is velocity,  $P$  is dynamic pressure,  $\eta$  is viscosity,  $\rho_m$  is the density of the ambient mantle,  $\Delta \rho_c$  is the compositional density anomaly,  $\mathbf{g}$  is the gravitational acceleration,  $T$  is temperature,  $\kappa$  is the thermal conductivity,  $C$  is chemical composition. More model-wise parameters are available in the supplementary material (Supplementary Table 1–3).

To reproduce natural, tabular, and asymmetrically subducting slabs that move freely and satisfy observed plate kinematics, we utilize a data-assimilation technique<sup>56–58</sup> that incorporates a recent plate reconstruction model<sup>3</sup>. The plate motion data from the reconstruction is imposed as surface boundary conditions in the time-dependent model and the bottom boundary is free to slip. The temperature profile of the oceanic lithosphere follows a modified error function<sup>57</sup> following the seafloor age from the reconstruction so that the slab buoyancy is the same as that in the actual Earth, while the continental lithosphere initiates with a steady-state temperature profile (Supplementary Fig. 1a). The core-mantle-boundary temperature is fixed to be 500 °C higher than the ambient mantle. The viscosity of the model depends on depth, temperature, and composition.

The models adopt a layered and smoothed background viscosity profile within 4 depth ranges: 0–44 km, 44–410 km, 410–660 km, and 660–2867 km. Their background viscosities are  $10^{20}$  Pa s,  $10^{20}$  Pa s,  $10^{21}$  Pa s and  $3 \times 10^{22}$  Pa s, respectively, and the reference viscosity is set to be  $10^{21}$  Pa s (Supplementary Fig. 1b). The temperature dependency of viscosity follows the equation:

$$\eta = \eta_0 \cdot C \cdot \exp\left(\frac{E_\eta}{T + T_\eta} - \frac{E_\eta}{T_m + T_\eta}\right) \quad (5)$$

where  $\eta_0$  is the background viscosity,  $C$  is the compositional viscosity variation,  $E_\eta$  is the activation energy,  $T$ ,  $T_\eta$  and  $T_m$  are the temperature, activation temperature, and ambient mantle temperature, respectively. The variation of viscosity is  $10^{19}$ – $10^{23}$  Pa s in the time-dependent model and  $10^{18}$ – $10^{24}$  Pa s in the instantaneous free-slip models that attempt to reproduce plate motion.

We consider a total of 13 different chemical compositions in the model (Supplementary Fig. 1d), represented by -1.8 billion tracers. The oceanic lithosphere is composed of a 7-km-thick surface layer that does not have buoyancy anomaly and only mimics the weak and lubricating plate interface near the trench during subduction, a 21-km-thick crustal layer whose buoyancy equals that of a 7-km-thick basaltic

crust, and the underlying lithospheric mantle. Both the oceanic basaltic crust and continental lower crust undergoes composition and density changes following the basalt-to-eclogite phase transformation at depths of -100 km. The continental lithosphere consists of 2 layers of crust and 3 layers of mantle lithosphere. The crust has an average density of  $\sim 2800 \text{ kg m}^{-3}$ , with the lower crust being weaker than the upper crust to mitigate the effect of deformation from the imposed plate motion to deeper depths. The continental mantle lithosphere consists of a buoyant upper layer, a neutrally buoyant middle layer, and a dense lower layer relative to the ambient mantle that follows recent inferences<sup>59–61</sup>. More compositional parameters are available in Supplementary Table 3. The entire continental lithosphere including the crust and the mantle lithosphere within a plate is mechanically coherent because of viscosity cut-off, while the weak zone fully decouples the plate boundary between two plates (Fig. 3c). This allows the stress accumulation in our model to occur primarily within the lithosphere as a whole rather than the crust alone. Thus, our lithospheric resolution is sufficient to capture the first-order force balance. Several recent studies<sup>27–33</sup> utilizing similar model resolution successfully capture 3D lithospheric stress state, deformation and topography.

### Generating plate motion

To reproduce plate motion and stress dynamically, we rerun the model using checkpoints stored at every 10 Myr. These reruns have the same mantle structures as in the sequential model but with a free-slip surface boundary condition. This way, internal mantle dynamics from slabs and plumes control the convective motion and drive deformation of the lithosphere, so that we can estimate the driving force of a given plate. Rigid rotation is removed during each rerun. We further remove the lithospheric net rotation from calculated plate motion for better comparison with observed plate motion in the NNR (no-net-rotation) frame. The mantle flow and stresses from the model with imposed plate motion are largely unchanged in the free-slip reruns<sup>31</sup>, validating the dynamic compatibility of the internal convection with observed surface kinematics. To achieve realistic plateness, we increase the viscosity of the lithosphere to  $10^{24}$  Pa s so that each plate moves as a coherent unit with little internal deformation. The viscosity of the oceanic asthenosphere is  $10^{18}$  Pa s and plate boundary viscosity is around  $10^{20}$  Pa s in order to mimic the effect due to strain-rate weakening<sup>62</sup>. These adjusted shallow viscosity features are not effectively constrained in the sequential simulation when imposed surface kinematics override the dynamics of these features. However, a proper representation of them in the free-slip reruns is crucial given their high sensitivity to plate motion and mantle dynamics.

### Quantification of mantle drag and boundary resistance

Mantle drag is a combination of friction drag and pressure drag. Friction drag is essentially the shear stress applied near the bottom of the lithosphere due to asthenospheric flow. The friction drag along plate motion direction follows the form:

$$F_f = - \int \int \frac{\tau_{r\theta} u_{p\theta} + \tau_{r\phi} u_{p\phi}}{|\mathbf{u}_p|} dA \quad (6)$$

where  $F_f$  is friction drag,  $\mathbf{u}_p$  is plate motion velocity,  $\tau$  is the stress,  $r$ ,  $\theta$ , and  $\phi$  are the radial, colatitudinal, and longitudinal direction, respectively, and  $A$  is the horizontal area. This value is positive for driving the plate motion and negative for resisting the plate motion. The stress used here is the maximum absolute value over depths near a viscosity-defined LAB (viscosity 10 times that of the background viscosity), from 0.75 times of this depth to 410 km.

Pressure drag is due to the blocking of horizontal mantle flow by the lithospheric step. This reflects the pressure gradient acting on the lithospheric step. Thus, computing pressure drag requires a 3D



integration of the pressure gradient over the lithospheric step direction as:

$$F_p = \int \int \int \frac{\omega(\mathbf{u}_p \cdot \mathbf{n})(\nabla P \cdot \mathbf{n})}{|\mathbf{u}_p|} dV \quad (7)$$

where  $F_p$  is pressure drag,  $\omega$  is a weighting function from the lithospheric step,  $\mathbf{n}$  is the lithospheric step normal vector (pointing to the lithospheric interior) and  $V$  is the volume of interest. Again, the positive value represents a driving force and vice versa. Before computing the integration, the algorithm goes through each depth of interest to find the distribution of the lithosphere (set as 1) and asthenosphere (set as 0) horizontally and acquire its gradient map (the lithospheric step),  $\mathbf{n}$  is the gradient unit vector and  $\omega$  is the scalar field of gradient amplitude normalized by the maximum value in the region of interest, ranging from 0 to 1.

During the calculation of plate driving force, we neglect the area within 300 km from the plate boundary to avoid potential boundary effect. To calculate the total force acting on the plate, we first convert the force, including friction drag and pressure drag, from each unit into torque, sum the torques together, and then convert the total torque back into an equivalent force using a reference vector. This reference vector points towards the center of the plate and has a length equal to the Earth's radius (6371 km). For comparison to traditional estimation of slab pull and ridge push, all the mantle drag forces (in the unit of  $N$ ) are divided by the square root of plate area in each time to give the unit of  $N m^{-1}$ .

Plate boundary resistant force is computed similar to pressure drag. The northern resistant force reveals as a dynamic pressure increase towards the Indo–Eurasia collision zone. Thus, we track the pressure force within 300 km and above a given latitude from the plate boundary to quantify northern boundary resistant force. The resistant force has different sign compared to driving force when projected to plate motion.

### Anisotropy calculation

We simulate the flow-induced seismic anisotropy based on the FORTRAN code DrexS<sup>56</sup> that considers the effect of dislocation creep, dynamic recrystallization, and grain boundary migration, similar to previous works<sup>29,63,64</sup>. The simulation initializes with randomly oriented mantle mineral aggregate that assumes 70% A-type olivine and 30% enstatite. These mineral aggregates advect and realign following the mantle flow from 20 Ma to the present day based on the free-slip models. This produces the full elastic tensors of the aggregates and, since the upper mantle is dominated by transverse isotropy, we use the symmetry axis of the transverse isotropy (TI axis) to represent the lattice-preferred orientation<sup>65</sup>.

### Test on free-slip and free-surface model

A regional 2D thermochemical model simulates continental collision driven by detached, sinking slabs in the lower mantle. We use the open-source software ASPECT<sup>66,67</sup> to solve the governing equations of conservation of mass, momentum, energy, and composition. An unstructured mesh resolves the 6000 × 2900 km numerical model domain with a grid resolution of 2.9 × 2.8 km maximum per element. Both experiments use visco-plastic non-Newtonian rheology laws. Both models run for a 0.4-Myr duration. The model includes creeping flow with thermal and chemical buoyancy forces, accounts for eclogite, olivine-spinel, and spinel-perovskite phase transitions, and considers the effects of adiabatic, shear, and radioactive heating.

Two numerical experiments were conducted with free-slip and free-surface boundary conditions for the upper surface, while all other conditions remain identical between the two models. The model prescribes two 2400-km-wide continental plates, separated by a 12-km-

wide weak zone in the middle, in the central top of the model. The gap between the plate edge and the model boundary is 600 km. Two vertical weak zones are set in the continental plates near the edges to ensure their motions are not artificially impeded by connecting to the boundary. A 900-km-wide, cold, and dense square-shaped sinking slab in the lower mantle drives the mantle flow that induces active continental collision. The slab has an effective density of 3500 kg m<sup>-3</sup>.

The model continental crust has a thickness of 41 km and consists of three layers. Felsic rheology of wet quartzite represents the upper (10 km thick) and middle (15 km thick) crust, whereas mafic rheology of plagioclase represents the lower crust (16 km thick). Anhydrous peridotite with the rheology of dry olivine represents the mantle.

The half-space cooling model with an age of 200 Myr defines the initial thermal structure of the continental lithosphere within 1500 km to the continental collision zone. To effectively simulate the effect of lithospheric step, we set the initial thermal structure for the further 900 km of the continental lithosphere to be equivalent to an age of 80 Myr. The initial temperature in the background mantle is 1300 °C plus an adiabatic gradient of 0.3 °C km<sup>-1</sup>.

In both models, all mechanical boundary conditions are free to slip, except for the model with a free top surface. The Arbitrary Lagrangian–Eulerian (ALE) method tracks the top surface for the model with a free-surface boundary condition. Erosion and sedimentation, according to the hillslope transport diffusion method with a coefficient of 10<sup>-8</sup> m<sup>2</sup> s<sup>-1</sup>, cause the evolution of this upper boundary.

The density of rocks varies with temperature  $T$  according to the equation:

$$\rho(T) = \rho_0 [1 - \alpha(T - T_0)] \quad (8)$$

where  $\rho_0$  is the reference density at  $T_0 = 298$  K, and  $\alpha$  is the thermal expansion coefficient.

The model considers the transformation of olivine to wadsleyite and ringwoodite and to bridgmanite in the mantle. An increase in the density of the crust to 3550 kg m<sup>-3</sup> considers the eclogization of the mafic lower continental crust. The model does not consider melting or hydration processes. The  $\rho_0$  for upper crust, middle crust, lower crust, and mantle are 2700, 2800, 3000 and 3300 kg m<sup>-3</sup>, respectively.

### Data availability

The seismic tomography model UUP-07 is available at <https://www.atlas-of-the-underworld.org/uu-p07-model/>. The seismic anisotropy model YB13SVani is available at <https://faculty.epss.ucla.edu/~cbeghein/research/global-tomography/sv-anisotropy-mantle-transition-zone/>.

Both plate reconstruction models from<sup>3</sup> and<sup>68</sup> are available via EarthByte (<https://www.earthbyte.org/category/resources/data-models/global-regional-plate-motion-models/>). The plate reconstruction model from<sup>69</sup> is available at <https://www.earthdynamics.org/earthmodel/page6.html>. The data generated in this study have been deposited to Zenodo at <https://doi.org/10.5281/zenodo.11364202>.

### Code availability

All figures are prepared with GMT (<https://www.generic-mapping-tools.org/>), Paraview (<https://www.paraview.org/>), and Matplotlib (<https://matplotlib.org/>). Surface velocity and plate boundary files are exported using GPlates (<https://www.gplates.org/>). The original version of CitcomS is available at [www.geodynamics.org/cig/software/citcoms/](http://www.geodynamics.org/cig/software/citcoms/). ASPECT is available at <https://aspect.geodynamics.org/>.

### References

- Molnar, P. & Tapponnier, P. Cenozoic tectonics of Asia: effects of a continental collision: features of recent continental tectonics in Asia can be interpreted as results of the India-Eurasia collision. *Science* **189**, 419–426 (1975).

2. Zahirovic, S. et al. Insights on the kinematics of the India-Eurasia collision from global geodynamic models. *Geochem. Geophys. Geosystems* **13**, 2011GC003883 (2012).
3. Müller, R. D. et al. Ocean basin evolution and global-scale plate reorganization events since pangea breakup. *Annu. Rev. Earth Planet. Sci.* **44**, 107–138 (2016).
4. Molnar, P. & Lyon-Caen, H. Some simple physical aspects of the support, structure, and evolution of mountain belts. in *Geological Society of America Special Papers vol. 218* 179–208 (Geological Society of America, 1988).
5. Molnar, P., England, P. & Martinod, J. Mantle dynamics, uplift of the Tibetan Plateau, and the Indian Monsoon. *Rev. Geophys.* **31**, 357–396 (1993).
6. Ghosh, A., Holt, W. E., Flesch, L. M. & Haines, A. J. Gravitational potential energy of the Tibetan Plateau and the forces driving the Indian plate. *Geology* **34**, 321 (2006).
7. Copley, A., Avouac, J. & Royer, J. India-Asia collision and the Cenozoic slowdown of the Indian plate: Implications for the forces driving plate motions. *J. Geophys. Res. Solid Earth* **115**, 2009JB006634 (2010).
8. Forsyth, D. & Uyeda, S. On the relative importance of the driving forces of plate motion. *Geophys. J. Int.* **43**, 163–200 (1975).
9. Turcotte, D. L. & Schubert, G. *Geodynamics*. (Cambridge University Press, Cambridge, United Kingdom, 2014).
10. Li, C., Van Der Hilst, R. D., Engdahl, E. R. & Burdick, S. A new global model for P wave speed variations in Earth's mantle. *Geochem. Geophys. Geosystems* **9**, 2007GC001806 (2008).
11. Amaru, M. Global Travel Time Tomography with 3-D Reference Models. *Geologica Ultraiectina* **274**, 174p (2007).
12. Capitanio, F. A., Morra, G., Goes, S., Weinberg, R. F. & Moresi, L. India-Asia convergence driven by the subduction of the Greater Indian continent. *Nat. Geosci.* **3**, 136–139 (2010).
13. Wang, Y., Zhang, L. & Li, Z.-H. Metamorphic densification can account for the missing felsic crust of the Greater Indian continent. *Commun. Earth Environ.* **3**, 166 (2022).
14. Chen, L., Capitanio, F. A., Liu, L. & Gerya, T. V. Crustal rheology controls on the Tibetan plateau formation during India-Asia convergence. *Nat. Commun.* **8**, 15992 (2017).
15. Li, J. & Song, X. Tearing of Indian mantle lithosphere from high-resolution seismic images and its implications for lithosphere coupling in southern Tibet. *Proc. Natl. Acad. Sci.* **115**, 8296–8300 (2018).
16. de Sigoyer, J. et al. Dating the Indian continental subduction and collisional thickening in the northwest Himalaya: Multichronology of the Tso Moriri eclogites. *Geology* **28**, 487–490 (2000).
17. Guillot, S. et al. Reconstructing the total shortening history of the NW Himalaya. *Geochem. Geophys. Geosystems* **4**, 2002GC000484 (2003).
18. Niu, Y. What drives the continued India-Asia convergence since the collision at 55 Ma? *Sci. Bull.* **65**, 169–172 (2020).
19. Stadler, G. et al. The dynamics of plate tectonics and mantle flow: from local to global scales. *Science* **329**, 1033–1038 (2010).
20. Capitanio, F. A. Current deformation in the Tibetan plateau: a stress gauge in the India-Asia collision tectonics. *Geochem. Geophys. Geosystems* **21**, e2019GC008649 (2020).
21. Bose, S., Schellart, W. P., Strak, V., Duarte, J. C. & Chen, Z. Sunda subduction drives ongoing India-Asia convergence. *Tectonophysics* **849**, 229727 (2023).
22. Zhou, X., Li, Z.-H., Gerya, T. V. & Stern, R. J. Lateral propagation-induced subduction initiation at passive continental margins controlled by preexisting lithospheric weakness. *Sci. Adv.* **6**, eaaz1048 (2020).
23. Bird, P. Testing hypotheses on plate-driving mechanisms with global lithosphere models including topography, thermal structure, and faults. *J. Geophys. Res. Solid Earth* **103**, 10115–10129 (1998).
24. Coltice, N., Husson, L., Faccenna, C. & Arnould, M. What drives tectonic plates? *Sci. Adv.* **5**, eaax4295 (2019).
25. Conrad, C. P. & Lithgow-Bertelloni, C. The temporal evolution of plate driving forces: Importance of “slab suction” versus “slab pull” during the Cenozoic. *J. Geophys. Res. Solid Earth* **109**, 2004JB002991 (2004).
26. Becker, T. W. & Faccenna, C. Mantle conveyor beneath the Tethyan collisional belt. *Earth Planet. Sci. Lett.* **310**, 453–461 (2011).
27. Peng, D. & Liu, L. Quantifying slab sinking rates using global geodynamic models with data-assimilation. *Earth-Sci. Rev.* **230**, 104039 (2022).
28. Peng, D., Liu, L. & Wang, Y. A newly discovered late-cretaceous East Asian flat slab explains its unique lithospheric structure and tectonics. *J. Geophys. Res. Solid Earth* **126**, e2021JB022103 (2021).
29. Peng, D., Liu, L., Hu, J., Li, S. & Liu, Y. Formation of East Asian stagnant slabs due to a pressure-driven cenozoic mantle wind following mesozoic subduction. *Geophys. Res. Lett.* **48**, e2021GL094638 (2021).
30. Li, Y., Liu, L., Peng, D., Dong, H. & Li, S. Evaluating tomotectonic plate reconstructions using geodynamic models with data assimilation, the case for North America. *Earth-Sci. Rev.* **244**, 104518 (2023).
31. Liu, Y. et al. Global back-arc extension due to trench-parallel mid-ocean ridge subduction. *Earth Planet. Sci. Lett.* **600**, 117889 (2022).
32. Cao, Z. & Liu, L. Origin of three-dimensional crustal stress over the conterminous United States. *J. Geophys. Res. Solid Earth* **126**, e2021JB022137 (2021).
33. Cao, Z., Liu, L. & Western, U. S. intraplate deformation controlled by the complex lithospheric structure. *Nat. Commun.* **15**, 3917 (2024).
34. Mao, W. & Zhong, S. Constraints on mantle viscosity from intermediate-wavelength geoid anomalies in mantle convection models with plate motion history. *J. Geophys. Res. Solid Earth* **126**, e2020JB021561 (2021).
35. Liu, L. & Gurnis, M. Simultaneous inversion of mantle properties and initial conditions using an adjoint of mantle convection. *J. Geophys. Res. Solid Earth* **113**, 2008JB005594 (2008).
36. Chen, L., Wang, X., Liang, X., Wan, B. & Liu, L. Subduction tectonics vs. Plume tectonics—Discussion on driving forces for plate motion. *Sci. China Earth Sci.* **63**, 315–328 (2020).
37. Ghosh, A. & Holt, W. E. Plate motions and stresses from global dynamic models. *Science* **335**, 838–843 (2012).
38. Zhong, X. & Li, Z. Wedge-shaped southern Indian continental margin without proper weakness hinders subduction initiation. *Geochem. Geophys. Geosystems* **23**, e2021GC009998 (2022).
39. Conrad, C. P. & Lithgow-Bertelloni, C. Influence of continental roots and asthenosphere on plate-mantle coupling. *Geophys. Res. Lett.* **33**, 2005GL025621 (2006).
40. Rudolph, M. L. & Zhong, S. J. History and dynamics of net rotation of the mantle and lithosphere. *Geochem. Geophys. Geosystems* **15**, 3645–3657 (2014).
41. Paul, J., Conrad, C. P., Becker, T. W. & Ghosh, A. Convective self-compression of cratons and the stabilization of old lithosphere. *Geophys. Res. Lett.* **50**, e2022GL101842 (2023).
42. Dongmo Wamba, M., Montagner, J.-P. & Romanowicz, B. Imaging deep-mantle plumbing beneath La Réunion and Comores hot spots: Vertical plume conduits and horizontal ponding zones. *Sci. Adv.* **9**, eade3723 (2023).
43. Ding, L. et al. Timing and mechanisms of Tibetan Plateau uplift. *Nat. Rev. Earth Environ.* **3**, 652–667 (2022).
44. Van Hinsbergen, D. J. J., Steinberger, B., Doubrovine, P. V. & Gassmüller, R. Acceleration and deceleration of India-Asia convergence since the Cretaceous: Roles of mantle plumes and continental collision. *J. Geophys. Res.* **116**, B06101 (2011).

45. Cande, S. C. & Stegman, D. R. Indian and African plate motions driven by the push force of the Réunion plume head. *Nature* **475**, 47–52 (2011).
46. Jagoutz, O., Royden, L., Holt, A. F. & Becker, T. W. Anomalously fast convergence of India and Eurasia caused by double subduction. *Nat. Geosci.* **8**, 475–478 (2015).
47. Kumar, P. et al. The rapid drift of the Indian tectonic plate. *Nature* **449**, 894–897 (2007).
48. Wang, W., Cawood, P. A., Pandit, M. K., Zhao, J.-H. & Zheng, J.-P. No collision between Eastern and Western Gondwana at their northern extent. *Geology* **47**, 308–312 (2019).
49. Liu, S. & King, S. D. Dynamics of the north american plate: large-scale driving mechanism from far-field slabs and the interpretation of shallow negative seismic anomalies. *Geochem. Geophys. Geosystems* **23**, e2021GCO09808 (2022).
50. Wan, B. et al. Cyclical one-way continental rupture-drift in the Tethyan evolution: subduction-driven plate tectonics. *Sci. China Earth Sci.* **62**, 2005–2016 (2019).
51. Li, Z. X. et al. Decoding Earth's rhythms: modulation of super-continent cycles by longer superocean episodes. *Precambrian Res* **323**, 1–5 (2019).
52. Zhong, S., Zhang, N., Li, Z.-X. & Roberts, J. H. Supercontinent cycles, true polar wander, and very long-wavelength mantle convection. *Earth Planet. Sci. Lett.* **261**, 551–564 (2007).
53. Cramer, F., Lithgow-Bertelloni, C. R. & Tackley, P. J. The dynamical control of subduction parameters on surface topography. *Geochem. Geophys. Geosystems* **18**, 1661–1687 (2017).
54. Zhong, S., Gurnis, M. & Moresi, L. Free-surface formulation of mantle convection-I. Basic theory and application to plumes. *Geophys. J. Int.* **127**, 708–718 (1996).
55. Zhong, S., Zuber, M. T., Moresi, L. & Gurnis, M. Role of temperature-dependent viscosity and surface plates in spherical shell models of mantle convection. *J. Geophys. Res. Solid Earth* **105**, 11063–11082 (2000).
56. Hu, J. & Liu, L. Abnormal seismological and magmatic processes controlled by the tearing South American flat slabs. *Earth Planet. Sci. Lett.* **450**, 40–51 (2016).
57. Liu, L. & Stegman, D. R. Segmentation of the Farallon slab. *Earth Planet. Sci. Lett.* **311**, 1–10 (2011).
58. Hu, J. et al. Modification of the Western Gondwana craton by plume–lithosphere interaction. *Nat. Geosci.* **11**, 203–210 (2018).
59. Zhou, Q., Liu, L., Hu, J. & Western, U. S. Volcanism due to intruding oceanic mantle driven by ancient Farallon slabs. *Nat. Geosci.* **11**, 70–76 (2018).
60. Wang, Y., Liu, L. & Zhou, Q. Geoid reveals the density structure of cratonic lithosphere. *J. Geophys. Res. Solid Earth* **127**, e2022JBO24270 (2022).
61. Wang, Y., Liu, L. & Zhou, Q. Topography and gravity reveal denser cratonic lithospheric mantle than previously thought. *Geophys. Res. Lett.* **49**, e2021GL096844 (2022).
62. Hu, J., Liu, L. & Gurnis, M. Southward expanding plate coupling due to variation in sediment subduction as a cause of Andean growth. *Nat. Commun.* **12**, 7271 (2021).
63. Hu, J., Faccenda, M. & Liu, L. Subduction-controlled mantle flow and seismic anisotropy in South America. *Earth Planet. Sci. Lett.* **470**, 13–24 (2017).
64. Zhou, Q. et al. Western U.S. seismic anisotropy revealing complex mantle dynamics. *Earth Planet. Sci. Lett.* **500**, 156–167 (2018).
65. Faccenda, M. & Capitanio, F. A. Seismic anisotropy around subduction zones: Insights from three-dimensional modeling of upper mantle deformation and SKS splitting calculations. *Geochem. Geophys. Geosystems* **14**, 243–262 (2013).
66. Heister, T., Dannberg, J., Gassmüller, R. & Bangerth, W. High accuracy mantle convection simulation through modern numerical methods – II: realistic models and problems. *Geophys. J. Int.* **210**, 833–851 (2017).
67. Rose, I., Buffett, B. & Heister, T. Stability and accuracy of free surface time integration in viscous flows. *Phys. Earth Planet. Inter.* **262**, 90–100 (2017).
68. Müller, R. D. et al. A global plate model including lithospheric deformation along major rifts and orogens since the Triassic. *Tectonics* **38**, 1884–1907 (2019).
69. Torsvik, T. H. et al. Pacific-panthalassic reconstructions: overview, errata and the way forward. *Geochem. Geophys. Geosystems* **20**, 3659–3689 (2019).
70. Yuan, K. & Beghein, C. Seismic anisotropy changes across upper mantle phase transitions. *Earth Planet. Sci. Lett.* **374**, 132–144 (2013).

## Acknowledgements

This work is supported by NSFC grant 92355302 to L.L., 42488201 to S.L., and Strategy Priority Research Program (Category B) of Chinese Academy of Sciences No. XDB0710000 to L.L. We are grateful to Jean-Philippe Avouac for his constructive comments. We also thank Fabio Capitanio for his helpful comments on an earlier draft.

## Author contributions

Y.L., L.L. and S.L. conceptualized the idea, Y.L. and L.L. drafted and reviewed the manuscript, Y.L. performed the main investigation and visualization, Y.L., L.L., S.L., D.P., Z.C., X.L. contributed to the methodology, analysis, and interpretation, L.L. supervised the project.

## Competing interests

The authors declare no competing interests.

## Additional information

**Supplementary information** The online version contains supplementary material available at <https://doi.org/10.1038/s41467-024-51107-0>.

**Correspondence** and requests for materials should be addressed to Lijun Liu or Sanzhong Li.

**Peer review information** *Nature Communications* thanks Jean-Philippe Avouac, and the other, anonymous, reviewer(s) for their contribution to the peer review of this work. A peer review file is available.

**Reprints and permissions information** is available at <http://www.nature.com/reprints>

**Publisher's note** Springer Nature remains neutral with regard to jurisdictional claims in published maps and institutional affiliations.

**Open Access** This article is licensed under a Creative Commons Attribution-NonCommercial-NoDerivatives 4.0 International License, which permits any non-commercial use, sharing, distribution and reproduction in any medium or format, as long as you give appropriate credit to the original author(s) and the source, provide a link to the Creative Commons licence, and indicate if you modified the licensed material. You do not have permission under this licence to share adapted material derived from this article or parts of it. The images or other third party material in this article are included in the article's Creative Commons licence, unless indicated otherwise in a credit line to the material. If material is not included in the article's Creative Commons licence and your intended use is not permitted by statutory regulation or exceeds the permitted use, you will need to obtain permission directly from the copyright holder. To view a copy of this licence, visit <http://creativecommons.org/licenses/by-nc-nd/4.0/>.

© The Author(s) 2024